

Metal–Semiconductor–Metal Ultraviolet Photodetectors Based on Al Nanoparticles in 4H-SiC Microholes

Meng Yuan, Mingkun Zhang,* Zhao Fu, Shan Han, Yuning Zhang, Shaoxiong Wu, Rongdun Hong, Xiaping Chen, Jiafa Cai, Dingqu Lin, Zhengyun Wu, Baoping Zhang,* Jicheng Wang,* and Feng Zhang*



Cite This: *ACS Appl. Nano Mater.* 2023, 6, 9376–9384



Read Online

ACCESS |



Metrics & More



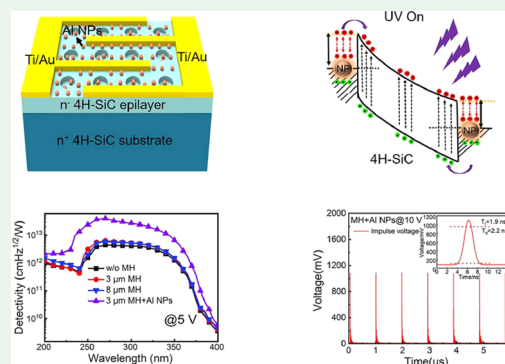
Article Recommendations



Supporting Information

ABSTRACT: A significant ultraviolet (UV) detection enhancement is realized by etching microhole (MH) arrays and localized surface plasmon resonance (LSPR) of Al nanoparticles (NPs) on 4H-SiC metal–semiconductor–metal (MSM) photodetectors (PDs). 4H-SiC PDs with different diameters of MHs are fabricated, which exhibit an ultralow dark current of approximately 5.0×10^{-15} A at 5 V bias. The PD with 3 μm MH exhibits the best performance, and its peak responsivity is 35% higher than that of device without MH. The peak responsivity of PDs with both 3 μm MH and NPs enhanced nearly 6 times that without Al NPs. The PD with both 3 μm MH and Al NPs indicates the best detection performance, with a maximum detectivity of 4.0×10^{13} Jones at 270 nm, which is nearly an order of magnitude higher than devices without Al NPs. The fabricated MH and Al NPs MSM PDs have a high response on the order of nanoseconds, with a rise/decay time of 2.1 ns/2.5 ns at 5 V bias. The complementary optical properties of MH and Al NPs with 4H-SiC can promote the development and application of high-performance UV PDs.

KEYWORDS: ultraviolet photodetector, silicon carbide, nanoparticles, microhole, plasmonic



INTRODUCTION

Ultraviolet (UV) photodetectors (PDs) are attracting much attention due to their wide application fields, such as ozone layer monitor, radar imaging, UV communication, and environmental monitoring.^{1–4} 4H-SiC-based PDs have been a long-standing interest in the UV detection research field due to their excellent material properties, including visible blindness, relatively mature processing technology, excellent chemical stability, and radiation hardness.⁵ Moreover, the band gap of 4H-SiC is 3.26 eV and the cutoff wavelength is around 380 nm. 4H-SiC UV PDs exhibit broad-band response characteristics in the UV spectral region. Therefore, there is no need to add filters to remove the influence of other light waves, and the application in the UV band will not be limited. MSM PDs are widely studied for the merits of low parasitic capacitance and easy fabrication for optoelectronic integrated circuits. However, 4H-SiC PDs suffered from low responsivity and quantum efficiency properties because of the low UV light absorption efficiency. In recent years, in order to further improve the performance of PDs, many methods had been used to improve the absorption efficiency including antireflection film,⁶ semitransparent electrode,⁷ microlens,⁸ nanowires,⁹ nanoholes,¹⁰ and nanorods.^{11,12} Microhole (MH) structure also has attracted much attention due to its facile preparation and high specific surface area under light conditions. Naderi et al. investigated the MH formation of

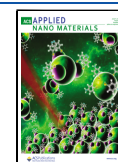
electrochemical corrosion SiC to enhance the detector performance.¹³ However, the geometric sizes of MHs are nonuniform and difficult to be regulated, and the surface roughness is high, which leads to a high dark current of the devices. Therefore, we prepare a regulable MH array by selective etching technique to enhance the UV light trapping.

On the other hand, nanoparticles (NPs) provide an accessible approach to significantly improve the UV PD performance.^{14–16} Localized surface plasmon resonance (LSPR) of metal NPs arising from light-induced oscillation of free electrons enhances the absorption and scattering of incident photons, which improves the photocurrent intensity and detectivity of optoelectronic devices.^{17–20} However, most applications have been demonstrated in the visible and infrared regions and only a few in the UV regions so far. Traditional noble metal NPs (e.g., Ag, Au, and Pt) with LSPR are normally in the visible region (Ag NPs: ~ 460 nm, Au NPs: ~ 520 nm; Pt NPs: ~ 400 nm),²¹ which severely limits their application in the UV region. Instead, Al with a high plasmon resonance energy

Received: March 10, 2023

Accepted: May 18, 2023

Published: May 29, 2023



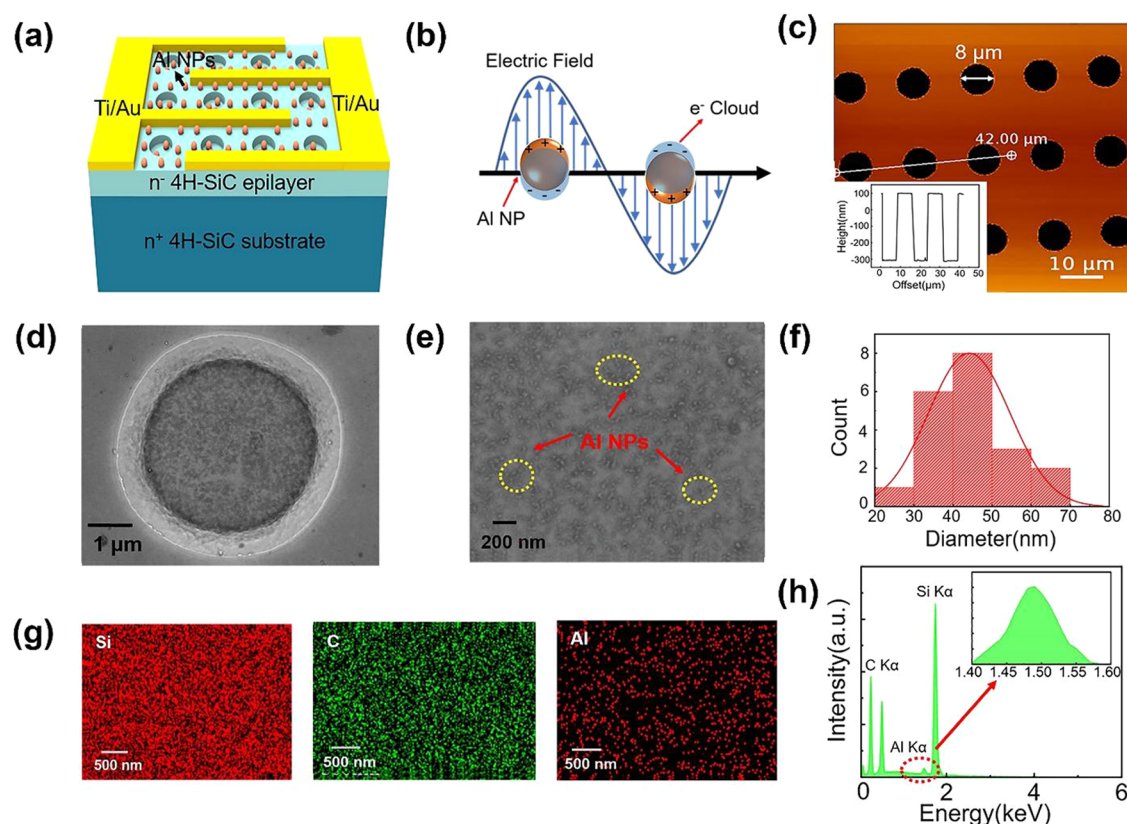


Figure 1. (a) Schematic diagram of the 4H-SiC MSM device with both MH and NPs. (b) Schematic of LSPR induced on the Al NPs by incident light. (c) Surface morphology of 8 μm MH arrays obtained by AFM measurement; the inset is the corresponding cross-sectional profile. (d) SEM image and (e) enlarged view of the MH surface after Al NPs deposition and annealing. (f) The size distribution histograms of Al NPs. (g) EDS elemental maps of Al NPs after annealing. (h) Corresponding EDS spectra.

of 15 eV is believed to be a potential candidate to reach the UV range.²² According to the Mie theory, the dielectric function of Al possesses a negative real part and relatively low imaginary part throughout the whole region,²³ suggesting an excellent potential to guarantee a superior plasmon resonance within the response wavelength range of 4H-SiC PDs. Liu et al. deposited the Al NPs on 4H-SiC MSM PDs by magnetron sputtering and obtained that the peak responsivity of devices is 3.93 times higher than that of devices without Al NPs.²⁴ In another study, an enhanced spectral response was also realized in AlGaN-based UV PDs with Al NPs.²⁵ However, MSM UV PDs using metal NPs typically suffer from low response speed, high dark current, and low detectivity, which greatly limits their application.

In this work, our purpose is to explore a new approach based on both MH structure and Al NPs LSPR to improve the performance of UV PDs. First, 4H-SiC MSM PDs with MH arrays are fabricated on a 4H-SiC epitaxial layer. Then, the self-assembled Al NPs are deposited on devices by electron beam evaporation, and high-performance 4H-SiC UV PDs are realized. Moreover, the mechanisms of MH arrays and plasmonic NPs on the properties of 4H-SiC MSM UV PDs are further explored by multiphysical simulation and optoelectronic measurements. This work demonstrates that the MH arrays and Al NPs could be applied to enhance absorption in the UV region due to their low cost (\sim \\$0.2) and high detectivity, which will support the improvement and practical application of UV optoelectronic devices. Thus, the

device could be widely used in space research, environmental testing, UV decontamination, and defense applications.

EXPERIMENT AND SIMULATION

Device Fabrication. A 4H-SiC epitaxial layer with a nitrogen doping concentration of $5.0 \times 10^{15} \text{ cm}^{-3}$ and a thickness of 10 μm , grown on the Si-face (0001) 4H-SiC substrate with a 4° off-axis toward the $\langle 11-20 \rangle$ direction, was used to fabricate the 4H-SiC MSM PDs. The epitaxial wafer was obtained from Dongguan Tianyu Semiconductor Technology Co., Ltd. The schematic diagram of the MSM device with Al NPs in MH is shown in Figure 1a. MH arrays with different diameters (including 0, 3, and 8 μm) were obtained by a combination of photolithography and inductively coupled plasma (ICP, SENTECH SI500) etching. Figure 1b shows the schematic of LSPR induced on the Al NPs by incident light. The detailed selective etching method is described as follows. First, a standard photolithography process is used to obtain the MH array patterns by using AZ5214E positive photoresist. Three kinds of MH diameters ($D = 0, 3, \text{ and } 8 \mu\text{m}$) were prepared, and the MH spacing is fixed to 7 μm . Subsequently, the inductively coupled plasma (ICP) etching was performed at 10 $^\circ\text{C}$ with a 30 sccm (CF_4)/5 sccm (O_2) gas flow rate; the substrate temperature is set at 10 $^\circ\text{C}$ to prevent photoresist degeneration caused by excessive temperature during the etching process, which will affect the subsequent photoresist removal. However, the cavity temperature would likely increase accordingly during the etching process due to plasma. The etching rate is controlled at 0.8 nm/s. Then, a lift-off process is

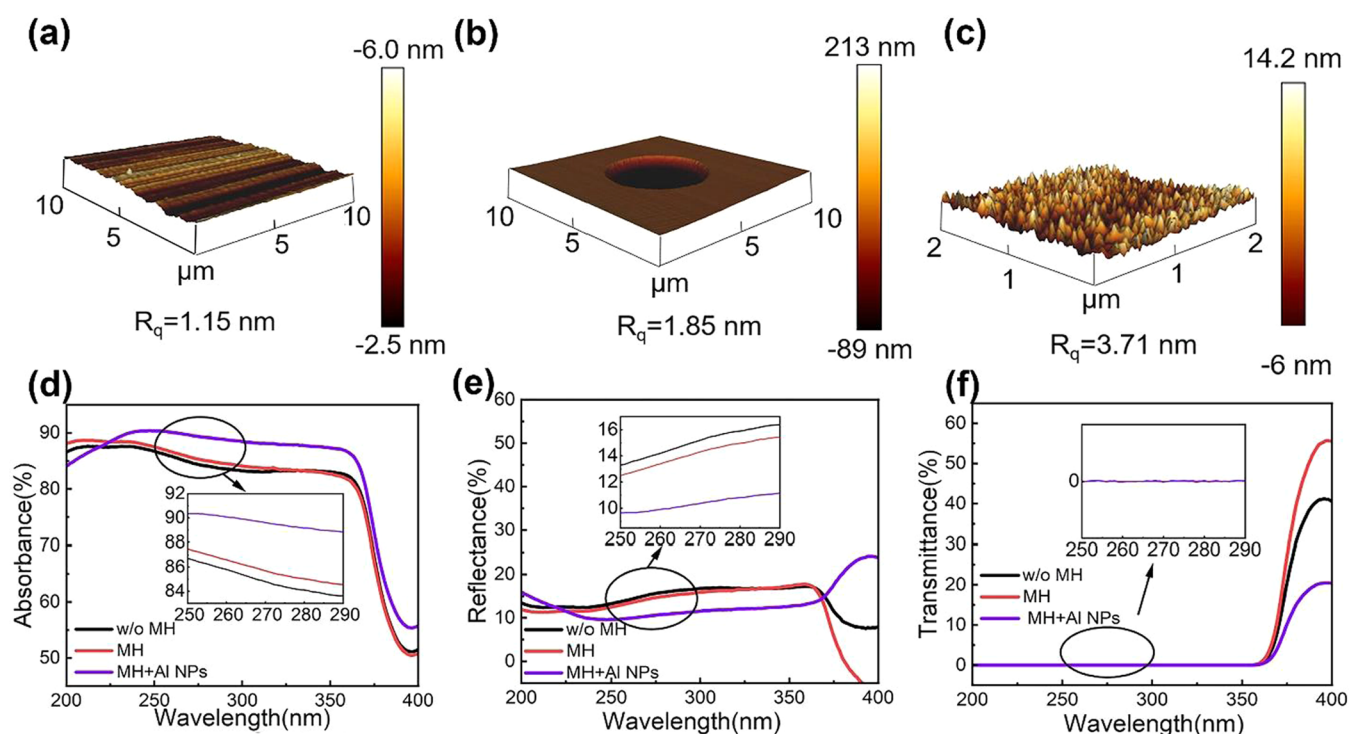


Figure 2. 3D-AFM side views of samples: (a) the surface morphology of bare SiC. (b) The surface morphology of MH. (c) The surface morphology of Al NPs after annealing. The optical analysis of the SiO₂/4H-SiC layer, the SiO₂/4H-SiC with MH, and the SiO₂/4H-SiC with Al NPs in MH. (d) Absorption spectra, (e) reflection spectra, and (f) transmission spectra.

applied to obtain the MH array. The surface morphology and corresponding cross-sectional profile of MHs were characterized by atomic force microscopy (AFM, Bruker NW4), as shown in Figure 1c. The MHs were arranged in order, showing a good shape after etching by ICP. The average depth of MHs was about 400 nm. To verify the impact of MH arrays on the response time of PD, we analyze the electric field depletion of different MH array devices (Figure S1 in the Supporting Information). Subsequently, samples were oxidized in wet/dry oxygen at 1150 °C for 5 h as a passivation and antireflection layer. After 5 h of oxidation, the thickness of the passivation and antireflection layer is 40–50 nm, which is enough to suppress the leakage current of the device effectively at low bias. The traditional 4H-SiC MSM PD without MH and Al NP also requires an oxidation process. The purpose of preparing the SiO₂ layer is to have a good passivation effect on the suspension bond on the surface of the device. Thermal oxidation and PECVD are the two methods to prepare the SiO₂ layer. Compared to the PECVD method, the SiO₂ film prepared by thermal oxidation has a higher density and a lower interface state density, which is beneficial to reduce the surface dark current of the device, especially the dark current at the MH.²⁶ The Ti/Au (40 nm/250 nm) was deposited by magnetron sputtering (Denton EXPLORER-14) as interdigital electrodes and pads. The finger width and spacing are both 10 μm, and the optical area is 7.2×10^{-2} mm². Next, a 5 nm thick Al layer was deposited on the sample surface using electron beam evaporation and the thickness of Al was controlled by directly tuning the power. Then, the samples were annealed at 500 °C for 2 h in high-purity N₂ ambient in order to form a good Schottky contact and self-assembled Al NPs. As a reference, the traditional 4H-SiC MSM PDs without MH and Al NPs were also fabricated using the same process. Figure 1d

shows the SEM image of the MH surface after Al NP deposition and annealing, and the corresponding enlarged view is shown in Figure 1e. According to the size distribution histogram of Al NPs, as shown in Figure 1f, the average diameter of Al NPs is 40–50 nm. The size of Al NPs is one of the main factors affecting the peak wavelength and local electric field distribution of LSPR. The peak wavelength of LSPR excitation can be determined from the far-field characteristic curve (Figures S2 and S3 in the Supporting Information). Meanwhile, the element distribution of the Al/SiC structures after annealing was analyzed by EDS as observed in Figure 1g. The Si, C, and Al are uniformly distributed throughout the whole structures, indicating the interdiffusion of Al atoms. The existence of Al can be further evidenced with the K α peak at 1.49 eV as shown with the EDS spectra in Figure 1h.

The absorption, reflection, and transmission spectra of the MH and Al NPs structure on 4H-SiC MSM PDs were obtained by UV–vis spectrophotometer (PerkinElmer Lambda 850). The current–voltage (*I*–*V*) characteristics of the 4H-SiC MSM PDs were measured by a probe station with a Keithley 4200-SCS parameter analyzer. As for the spectral responsivity measurement, a xenon lamp as the light source was dispersed by a monochromator for wavelength selection, and the devices under test were illuminated from the front by monochromatic light transmitted through the fiber. The incident light power was calibrated with a Si-based detector in the wavelength range from 200 to 400 nm. Figure S4 (in the Supporting Information) shows the power density profile of incident light in the wavelength range from 200 to 400 nm.

Simulation Method. Optoelectronic simulation (COM-SOL) was used to calculate and analyze the electric field distribution and absorption performance of MH arrays with

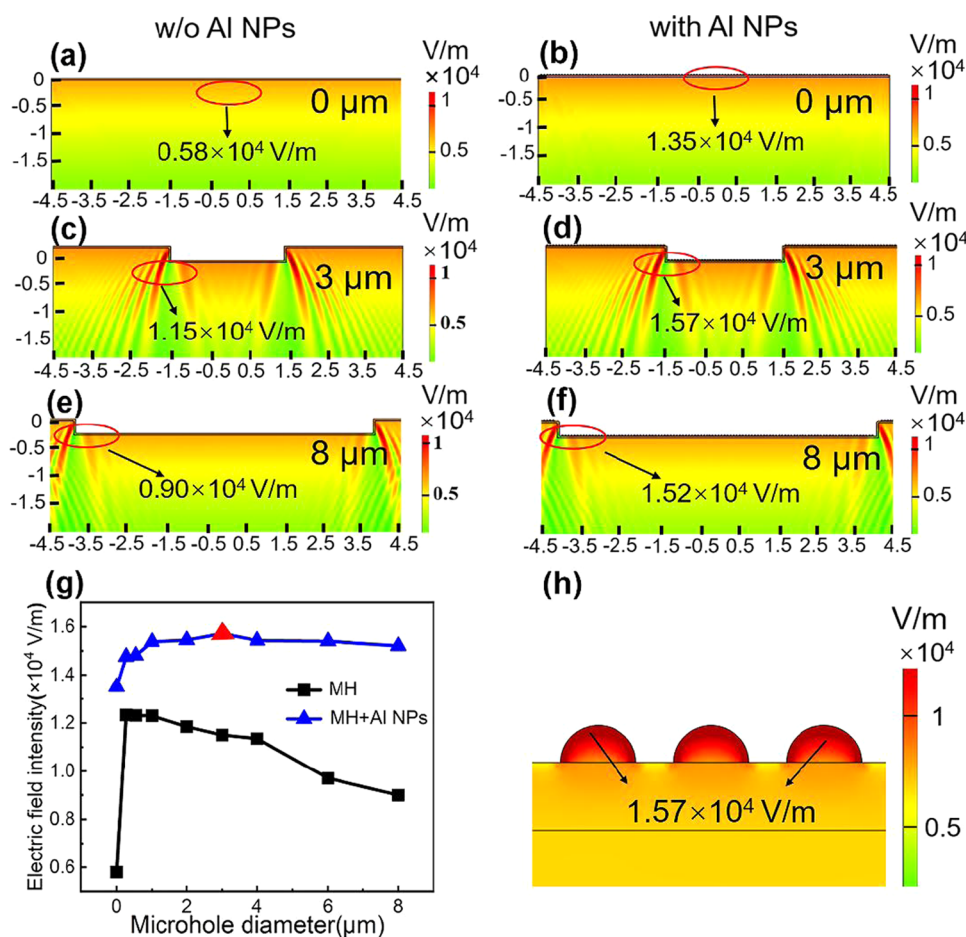


Figure 3. Electric field distribution of devices with different MH diameters under the condition of without and with Al NPs: panels (a) and (b) are without MH. Panels (c) and (d) are 3 μm MH. Panels (e) and (f) are 8 μm MH. (g) The peak electric field intensity with different MH diameters. (h) Enlarged view of Al NPs on the MH surface.

different diameters and optimized the surface to improve the performance of UV detectors. The “wave optics module” provides a traditional full-wave propagation method based on the direct discretization of Maxwell’s equations. Maxwell’s equations can be solved by establishing the corresponding finite element model, so the relevant electromagnetic field intensity (E and H) and electric flux density (D and B) can be obtained from the solution in this simulation field. To describe the real-space photoelectric field distribution of the structure, COMSOL was used to numerically solve the Maxwell equation.

Because of the periodic structure of the MH arrays, in order to reduce the workload and complexity of calculation, the periodic port and periodic boundary of the software were combined to make the simulated region become a periodic arrangement and hence only need to simulate one of these cells. To simulate the propagation of incident light in the simulation region in the real scene, the perfect matching layer (PML) thickness of 200 nm is defined at the top and bottom of the simulation region. A broad-band pulse in the wavelength range of 200–400 nm was used to simulate a plane wave incident from the top. The incident power from the UV source was set at 1.0 W. By adding the PML, the nonmeaningful reflections and interference caused by reflected light in the simulation area can be eliminated.

RESULTS AND DISCUSSION

Figure 2 shows the morphological and optical properties of the bare 4H-SiC, the $\text{SiO}_2/4\text{H-SiC}$ with MH, and the $\text{SiO}_2/4\text{H-SiC}$ with Al NPs in MH. The surface morphology of each sample is demonstrated by the 3D-AFM side view. As shown in Figure 2a, the surface of bare SiC showed a smooth step texture on the surface. With the preparation of MH arrays and Al NPs on samples, the MH and uniformly distributed Al NPs were formed, as displayed in Figure 2b,c. Furthermore, the optical properties of the $\text{SiO}_2/4\text{H-SiC}$ layer, $\text{SiO}_2/4\text{H-SiC}$ with MH, and $\text{SiO}_2/4\text{H-SiC}$ with Al NPs in MH were studied by the absorption, reflection, and transmission spectra, as shown in Figure 2d–f. The experimental results show that for the short wavelength below 255 nm, different structures have little effect on absorptivity. This is due to the incident light decaying in the shallow surface area because of the high absorption coefficient of 4H-SiC, resulting in little difference in the light field distribution, and the change of MH diameter has little effect on the electric field. However, the MH structure and Al NPs in MH increase the UV light absorption in the wavelength range of 255–360 nm. The reason is that the light-trapping effect of the MH structure and the presence of Al NPs increase surface roughness, further increasing the scattering and absorption of incident photons. Since there is no difference in transmittance, compared to the device without MH, the absorption of the device with MH and the device with Al

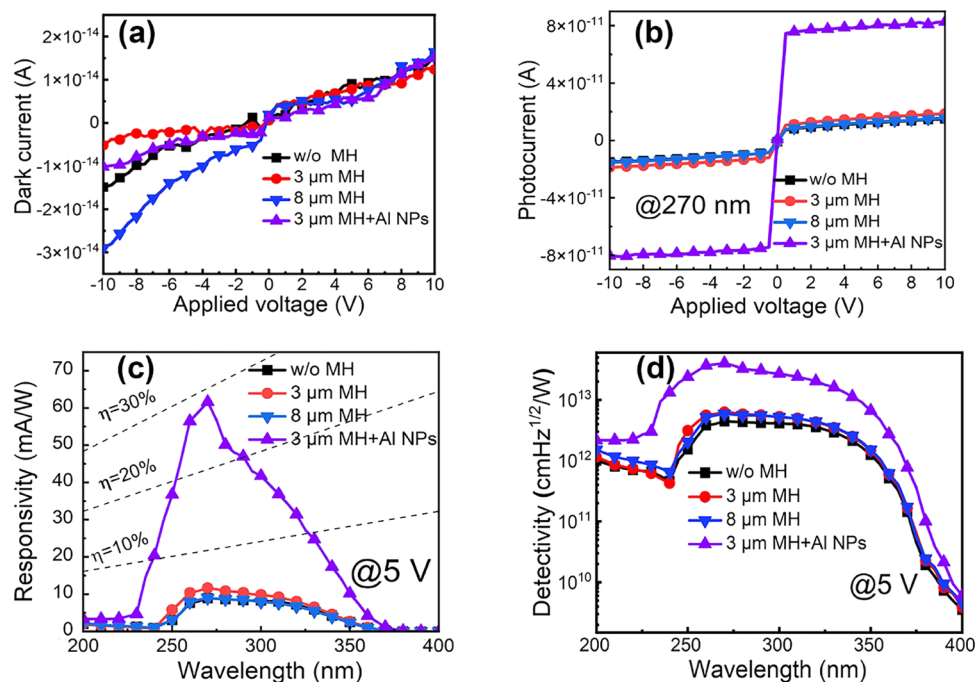


Figure 4. Electrical and optical characteristics of devices without MH, with 3 μm MH, with 8 μm MH, and with both 3 μm MH and Al NPs. (a) Dark current–voltage characteristics. (b) Photocurrent–voltage characteristics. (c) Spectral response. (d) Specific detectivity characteristics.

MH increases by 2.3 and 7.1%, respectively, so the corresponding reflectance is also different.

The results can be reasonably explained by the electric field distribution of the MH structure shown in Figure 3a–g. The cross-sectional electric field distributions of samples are simulated. The left panel (Figure 3a,c,e) shows the electric field distribution of the MH structure without Al NPs. Figure 3a shows the traditional structure without MH and NPs, while Figure 3c,e shows the MHs alone with the diameters of 3 and 8 μm , respectively. More simulation results of MH structures with different diameters are shown in Figure 3g. In addition, the entire right panel shows the electric field distribution of the MH structure with Al NPs. Since the size of Al NPs is much smaller than the diameter of the MH structure, an enlarged schematic of Al NPs at the MH is shown in Figure 3h, which shows the electric field distribution with Al in MHs.

The electric field intensity in the near-surface area of the MH pattern is much larger than that of the plane area, which can be attributed to its low optical density and geometric antireflection effect of guided mode excitation.^{27,28} The vertical stripes are used to describe the propagation process of incident waves and represent the field distribution in the propagation process. All of the MH structures show an obvious enhancement of electric field intensity. In contrast, the field intensity of planar SiC decays exponentially as a function of distance from the surface. This indicates that the MHs concentrate the incident light into the MH area. Thus, more photogenerated carriers are created close to a space charge region with a higher collection probability than those in the region without MH, leading to enhanced quantum efficiency performance.²⁹ However, Figure 3g shows that the electric field intensity decreases with the increase of the MH diameter. This phenomenon can be attributed to the poor light-trapping effect caused by the larger aspect ratio of MH. It can be found that the devices with Al NPs in MH obtained a higher electric field intensity compared to the devices only with MHs, which

is due to enhanced scattering and absorption of incident photons by surface plasmons. Moreover, the devices with both 3 μm MH and Al NPs obtained the largest electric field intensity. With the increase of the diameter of MH, although the light-trapping effect becomes worse, more surface plasmons will promote further absorption of incident light. The devices with both 3 μm MH and Al NPs obtained the largest electric field intensity, which is probably due to the combined effect of light trapping and surface plasmons. Therefore, in Figure 2d–f, the structure of Al NPs in MH has a significantly increased absorption of UV light in the wavelength range from 255 to 360 nm.

The four kinds of 4H-SiC MSM PDs, including without MH, with 3 μm MH arrays, with 8 μm MH arrays, and with both 3 μm MH and Al NPs, were fabricated and measured. Figure 4a,b shows the dark current and photocurrent–voltage characteristics of the fabricated PDs measured at room temperature in the bias range from -10 to 10 V. All devices exhibit an ultralow dark current (I_d) of about 5×10^{-15} A under 5 V bias as shown in Figure 4a. This is mainly due to the improvement of the thermal oxidation process during the experiment, which reduces the surface density of states at the interface. The SiO_2 passivation layer on the 4H-SiC surface effectively suppressed the dark current formed by surface leakage under low and medium bias voltages. However, the dark current curve is not very symmetrical; there are two main reasons: (1) the device will be charged and discharged during the application bias due to the internal charge of the oxide layer itself and (2) the position of the microholes may not be exactly in the center of the interdigital electrodes due to the lithography deviation, which result in the different charge collection efficiencies for the anodes and cathodes. In the meantime, the PDs with 8 μm MH present a higher dark current under reverse bias, which is mainly due to the increase of the etching area. The surface damage at the microhole increases due to the etching process damage, thus showing a

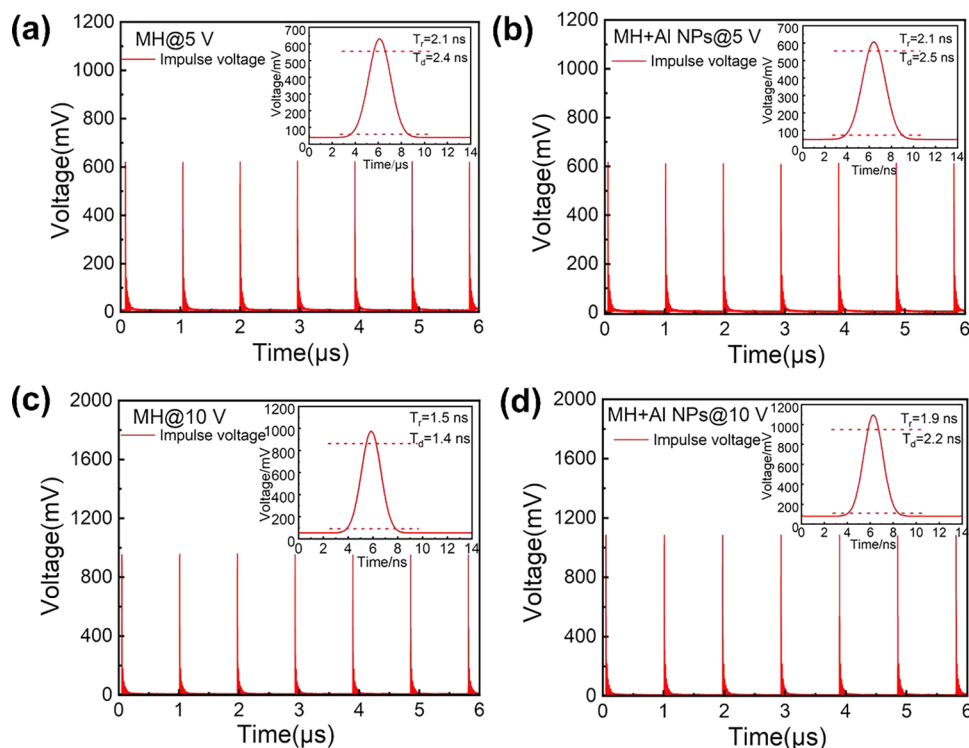


Figure 5. Temporal photoresponse of MSM PDs at different biases: (a) 3 μm MH at 5 V, (b) both 3 μm MH and Al NPs at 5 V, (c) 3 μm MH at 10 V, and (d) both 3 μm MH and Al NPs at 10 V. The inset is a magnification of a single impulse.

higher dark current than other devices. Photosensitivity (S) is a substantial parameter in governing the quality of the fabricated PDs. It is defined as the ratio of the photocurrent per measured dark current, which can be expressed as eq 1

$$S = \frac{I_{\text{ph}} - I_{\text{d}}}{I_{\text{d}}} \quad (1)$$

where I_{ph} and I_{d} represent the photocurrent and dark current of fabricated PDs, respectively.

The photocurrent–voltage characteristics of the devices are measured under UV light illuminations at 270 nm. The photocurrent of devices with both 3 μm MH and Al NPs increases greatly, which is about 6 times higher than that of devices with MH, as shown in Figure 4b. The photosensitivity of devices with Al NPs is 1.6×10^4 @ 5 V bias. Through the test spectrum of Figure 2, it can be seen that compared with the devices without MH, the photocurrent of devices with the MH structure is improved because of the geometric antireflection effect, while the reason for the greater photocurrent of 3 μm MH compared with that for 8 μm MH is that the transverse and vertical ratios of MH are larger, making its geometric antireflection effect more significant. The highest photocurrent of devices with both 3 μm MH and Al NPs is mainly due to the presence of Al NPs, which further increases the scattering and absorption of incident photons. At the same time, due to the excitation of the surface plasmon of Al NPs, the electromagnetic fields on the Al NPs can also be enhanced due to the collective oscillation of electrons and the excited hot electrons from the Al NPs spontaneously transfer to the conduction band of SiC, thus significantly increasing the photocurrent of the devices.

The device performance was further evaluated by determining the figure of merit parameters for PDs such as responsivity

(R) and specific detectivity (D^*). The R and D^* can be calculated by the following formulas

$$R = \frac{I_{\text{p}}}{P_{\text{opt}}} = \frac{I_{\text{ph}} - I_{\text{d}}}{P_{\text{opt}}} \quad (2)$$

$$D^* = R \times \sqrt{A/(2eI_{\text{d}})} \quad (3)$$

where I_{ph} and I_{d} represent the photocurrent and dark current of fabricated PDs, respectively. P_{opt} is the optical power in watts. e is the free electron charge and A represents the effective illuminated area. The I_{ph} is about three orders of magnitude higher than I_{d} for any PDs ($I_{\text{ph}} - I_{\text{d}} \approx I_{\text{ph}}$); therefore, the responsivity depends linearly on I_{ph} .

Figure 4c shows that the responsivity of devices with both 3 μm MH and Al NPs is significantly enhanced in the wavelength range from 230 to 350 nm. The device has a peak responsivity of 63 mA/W at 270 nm under 5 V bias, which is a 600% increase compared to devices only with MH. The responsivity is greatly enhanced with the incorporation of Al NPs. In addition, the external quantum efficiency (η) is defined by the ratio of the photocurrent to the incident photon flux. The devices with both 3 μm MH and Al NPs have a quantum efficiency of up to nearly 30%.

Besides, the ability of devices to detect weak signal is usually represented by specific detectivity. The specific detectivity of the four MSM PDs biased at 5 V is shown in Figure 4d. The devices with both 3 μm MH and Al NPs indicate the best detection performance; it can be seen from eq 3 that the D^* is closely related to the responsivity and dark current of the devices. The fabricated SiO_2 passivation layer effectively suppresses the leakage current, and the Al NPs enhance the responsivity of the devices. The highest D^* of devices with both 3 μm MH and Al NPs is 4.0×10^{13} Jones at 270 nm,

Table 1. Summary of Performance Parameters of SiC MSM PDs

materials	I_d (A)	R (A/W)	D^* (Jones)	T_r (ms)	T_d (ms)	references
Al NPs/4H-SiC	5.0×10^{-15}	0.063	4.0×10^{13}	1.9×10^{-6}	2.2×10^{-6}	this work
Al NPs/4H-SiC	2.1×10^{-11}	0.165	2.3×10^{12}			24
4H-SiC MSM	4.5×10^{-13}	0.094	7.8×10^{12}			29
4H-SiC MSM	2.4×10^{-9}	0.07	3.35×10^9			30
4H-SiC MSM	5.6×10^{-9}	0.0001	8.18×10^7	28	45.6	31

which is nearly an order of magnitude higher than that of devices only with 3 μm MH. This is mainly attributed to the combination of the MH structure and Al NP plasmon. On the one hand, the incident light on the MH structure causes diffraction of the incident light, increases the internal optical path, and enhances the absorption efficiency. On the other hand, the plasmon effect of Al NPs further increases the scattering absorption of the incident light and causes local field enhancement. This indicates that the fabricated devices have a high ability to characterize the normalized signal-to-noise performance.

Figure 5 indicates the temporal photoresponse of MSM PDs with MH alone and with both MH and Al NPs. The light with a wavelength of 266 nm is excited by using a picosecond pulsed laser, with a pulse width of 10 ps and a recurrence frequency at 1×10^6 Hz. Then, a Keithley 2410 sourcemeter and an oscilloscope (Tektronix MSO44) were used to measure the voltage transient response of the PDs. The rise time and decay time are defined at 10–90 and 90–10% of the value, respectively. As shown in Figure 5a,b, the rise/decay time of 3 μm MH and Al NPs in MH MSM PDs can be estimated to be 2.1 ns/2.4 ns and 2.1 ns/2.5 ns at 5 V, respectively. When the test voltage is increased to 10 V, there is also no significant difference in the rise/decay time, as shown in Figure 5c,d. The devices with both MH and Al NPs have a temporal response on the order of nanoseconds, which is expected to respond to the high-speed UV signals in real time. The response time refers to the time it takes for the light to be incident onto a device to generate a photocurrent in an electron–hole pair. The response time is usually affected by the diffusion time of the carriers, the crossing time of the carriers, etc. The reasons for the high response speed include two main points: first, the device with a 10 μm finger spacing can be completely depleted in the horizontal. Therefore, carriers are collected by the electrode through drift rather than diffused, which results in a higher response speed; second, 4H-SiC has a shorter minority carrier lifetime (hundreds of nanoseconds) compared with other materials, which leads to a higher response speed. Under different bias conditions, the temporal photoresponse of MSM PDs with both MH and Al NPs is delayed compared with that of devices with MH alone, mainly due to the delay effect on incident photons generated by the Al NP excited plasmon resonance. Table 1 summarizes the performance parameters for MSM PDs. Compared with other reported studies, the fabricated 4H-SiC MSM PDs have a lower dark current and higher detection sensitivity and higher response speed.

In terms of the interaction of incident UV photons with NPs and energy band theory, the mechanism associated with the responsivity enhancement of UV PDs by plasmonic NPs is further explored. As shown in Figure 6a, under the condition of without UV illumination and bias, the surface plasmon resonance of Al NPs cannot be excited. Since the metal electrodes are all Ti/Au, the Schottky barrier with a height of about 1.11 eV is formed.³² As shown in Figure 6b, under UV

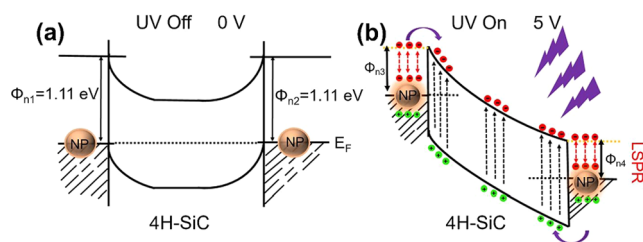


Figure 6. (a) Schematic of the energy band diagrams of the 4H-SiC MSM PDs with Al NPs. (b) The charge-transfer process between 4H-SiC and Al NPs at 5 V.

illumination and the applied bias conditions, a Schottky contact should be formed between Al NPs and 4H-SiC because the work function of Al is higher than the n-type 4H-SiC, which results in a localized depletion region between the 4H-SiC surface and Al NPs. Therefore, incident photons, especially those with a wavelength of less than 380 nm, can be better absorbed and separated into electrons and holes under the action of the localized depletion region. The photo-generated electrons are rapidly swept away by the electric field, while the holes remain self-trapped in the depletion region,³³ reducing the Schottky barrier height, which is now about 1.07 eV. Hot electrons with a much higher energy than the carriers near the Fermi energy by the excited surface plasmon in Al NPs under UV light irradiation thereby overcome the barrier height to reach the plasma band and spontaneously transfer to the conduction band of SiC. Moreover, the incident UV light irradiation and Al NP excitation of LSPR can not only increase light absorption but also accelerate the separation of photogenerated carriers more effectively, resulting in a significant increase in photocurrent.³⁴ On the contrary, for the devices without Al NPs, more free electrons and holes are likely to be recombined by surface defects due to the lack of the Schottky junction depletion region, resulting in a decrease of responsivity. Therefore, the photocurrent of fabricated 4H-SiC PDs with plasmonic NPs can be largely enhanced.

CONCLUSIONS

In summary, we have demonstrated Al-localized surface plasmon-enhanced 4H-SiC MSM UV PDs with regulable MH arrays. Devices with both MH and Al NPs exhibit a peak responsivity of 63 mA/W at 270 nm under a 5 V bias, representing a 600% increase compared to devices with MH alone. The highest D^* is 4.0×10^{13} Jones at 270 nm, which is nearly an order of magnitude higher than devices without Al NPs. Meanwhile, compared with other plasmonic-enhanced PDs, the 4H-SiC MSM PDs with MH and Al NPs enabled a lower dark current and a high temporal response on the order of nanoseconds. The MH and plasmonic-enhanced 4H-SiC-based UV PDs reported here may provide a low-cost and efficient method to achieve excellent PD performance.

■ ASSOCIATED CONTENT

SI Supporting Information

The Supporting Information is available free of charge at <https://pubs.acs.org/doi/10.1021/acsnm.3c01080>.

Electric field mapping of the device without MH, with 3 μm MH, and 8 μm MH at 5 V simulated by TCAD; the electric field intensity of the three devices at the same position; extinction spectra of Al nanoparticles with different sizes in the wavelength range of 200–700 nm; extinction spectra of Al NPs with different thicknesses in the wavelength range of 200–700 nm; the radial size of the NPs is fixed at (a) $D = 40$ nm and (b) $D = 50$ nm; and the power density profile of the incident light in the range of 200–400 nm (PDF)

■ AUTHOR INFORMATION

Corresponding Authors

Mingkun Zhang – Department of Physics, Xiamen University, Xiamen 361005, China; Jiujiang Research Institute of Xiamen University, Jiujiang 332000, China; Email: mkzhang@xmu.edu.cn

Baoping Zhang – School of Electronic Science and Engineering, Xiamen University, Xiamen 361005, China; Email: bzhang@xmu.edu.cn

Jicheng Wang – School of Science, Jiangnan University, Wuxi 214122, China; orcid.org/0000-0003-2814-2302; Email: jcwang@jiangnan.edu.cn

Feng Zhang – Department of Physics, Xiamen University, Xiamen 361005, China; Jiujiang Research Institute of Xiamen University, Jiujiang 332000, China; Email: fzhang@xmu.edu.cn

Authors

Meng Yuan – Department of Physics, Xiamen University, Xiamen 361005, China

Zhao Fu – Department of Physics, Xiamen University, Xiamen 361005, China

Shan Han – Department of Physics, Xiamen University, Xiamen 361005, China

Yuning Zhang – Department of Physics, Xiamen University, Xiamen 361005, China

Shaoyong Wu – Department of Physics, Xiamen University, Xiamen 361005, China

Rongdun Hong – Department of Physics, Xiamen University, Xiamen 361005, China; Shenzhen Research Institute of Xiamen University, Shenzhen 518057, China

Xiaping Chen – Department of Physics, Xiamen University, Xiamen 361005, China

Jiafa Cai – Department of Physics, Xiamen University, Xiamen 361005, China

Dingqu Lin – Department of Physics, Xiamen University, Xiamen 361005, China

Zhengyun Wu – Department of Physics, Xiamen University, Xiamen 361005, China

Complete contact information is available at: <https://pubs.acs.org/doi/10.1021/acsnm.3c01080>

Notes

The authors declare no competing financial interest.

■ ACKNOWLEDGMENTS

This research was supported by the National Natural Science Foundation of China (Grant No. 62274137), the Natural Science Foundation of Fujian Province of China for Distinguished Young Scholars (Grant No. 2020J06002), The Natural Science Foundation of Jiangxi Province of China for Distinguished Young Scholars (No. S2021QNZD2L0013), the Science and Technology Project of Fujian Province of China (Grant No. 2020I0001), the Science and Technology Key Projects of Xiamen (Grant No. 3502ZCQ20191001), the Laboratory Open Fund of Beijing Smart-chip Microelectronics Technology Co., Ltd. (Grant No. SGSC0000KJQT2207192), the Fundamental Research Funds for the Central Universities (Grant No. 20720220026), the Shenzhen Science and Technology Program (Grant No. JSGG20201102155800003), and the Jiangxi Provincial Natural Science Foundation (Grant No. 20212ACB212005).

■ REFERENCES

- (1) Chen, H. Y.; Liu, K. W.; Hu, L. F.; Al-Ghamdi, A. A.; Fang, X. S. New concept ultraviolet photodetectors. *Mater. Today* **2015**, *18*, 493–502.
- (2) Zhang, Y.; Cai, Y.; Zhou, J.; Xie, Y.; Xu, Q. W.; Zou, Y.; Guo, S. S.; Xu, H. X.; Sun, C. L.; Liu, S. Surface acoustic wave-based ultraviolet photodetectors: a review. *Sci. Bull.* **2020**, *65*, 587–600.
- (3) Huang, C.; Zhang, H. C.; Sun, H. D. Ultraviolet optoelectronic devices based on AlGaIn-SiC platform: Towards monolithic photonics integration system. *Nano Energy* **2020**, *77*, No. 105149.
- (4) Zheng, W.; Jia, L. M.; Huang, F. Vacuum-Ultraviolet Photon Detections. *iScience* **2020**, *23*, 22–23.
- (5) Monroy, E.; Omnes, F.; Calle, F. Wide-bandgap semiconductor ultraviolet photodetectors. *Semicond. Sci. Technol.* **2003**, *18*, R33–R51.
- (6) Zhang, F.; Yang, W. F.; Huang, H. L.; Chen, X. P.; Wu, Z. G.; Zhu, H. L.; Qi, H. G.; Yao, J. K.; Fan, Z. X.; Shao, J. D. High-performance 4H-SiC based metal-semiconductor-metal ultraviolet photodetectors with $\text{Al}_2\text{O}_3/\text{SiO}_2$ films. *Appl. Phys. Lett.* **2008**, *92*, No. 251102.
- (7) Sun, C. Z.; Chen, X. F.; Hong, R. D.; Li, X. M.; Xu, X. G.; Chen, X. P.; Cai, J. F.; Zhang, X. A.; Cai, W. W.; Wu, Z. Y.; Zhang, F. Enhancing the photoelectrical performance of graphene/4H-SiC/graphene detector by tuning a Schottky barrier by bias. *Appl. Phys. Lett.* **2020**, *117*, No. 071102.
- (8) Zhu, T. F.; Liu, Z. C.; Liu, Z. C.; Li, F. N.; Zhang, M. H.; Wang, W.; Wen, F.; Wang, J. J.; Bu, R. A.; Zhang, J. W.; Wang, H. X. Fabrication of monolithic diamond photodetector with microlenses. *Opt. Express* **2017**, *25*, 31586–31594.
- (9) Zhang, X. L.; Liu, Q. Y.; Liu, B. D.; Yang, W. J.; Li, J.; Niu, P. J.; Jiang, X. Giant UV photoresponse of a GaN nanowire photodetector through effective Pt nanoparticle coupling. *J. Mater. Chem. C* **2017**, *5*, 4319–4326.
- (10) Han, S. E.; Chen, G. Optical Absorption Enhancement in Silicon Nanohole Arrays for Solar Photovoltaics. *Nano Lett.* **2010**, *10*, 1012–1015.
- (11) Zheng, H. R.; Jiang, Y. R.; Yang, S. Y.; Zhang, Y.; Yan, X. F.; Hu, J. M.; Shi, Y. S.; Zou, B. S. ZnO nanorods array as light absorption antenna for high-gain UV photodetectors. *J. Alloys Compd.* **2020**, *812*, No. 152158.
- (12) Zhangyang, X. Y.; Liu, L.; Lv, Z. S.; Lu, F. F.; Tian, J. Comparative analysis of light trapping GaN nanohole and nanorod arrays for UV detectors. *J. Nanopart. Res.* **2020**, *22*, No. 243.
- (13) Naderi, N.; Moghaddam, M. Ultra-sensitive UV sensors based on porous silicon carbide thin films on silicon substrate. *Ceram. Int.* **2020**, *46*, 13821–13826.
- (14) Wu, Y.; Sun, X. J.; Shi, Z. M.; Jia, Y. P.; Jiang, K.; Ben, J. W.; Kai, C. H.; Wang, Y.; Lu, W.; Li, D. B. In situ fabrication of Al surface plasmon nanoparticles by metal-organic chemical vapor deposition for

enhanced performance of AlGaIn deep ultraviolet detectors. *Nanoscale Adv.* **2020**, *2*, 1854–1858.

(15) Cao, F.; Ji, X. H. Enhanced self-powered UV sensing performance of ZnO/Au/Al₂O₃ photodetector with the decoration of Au nanoparticles. *J. Mater. Sci.-Mater. Electron.* **2020**, *31*, 2657–2665.

(16) Kunwar, S.; Pandit, S.; Jeong, J. H.; Lee, J. Improved Photoresponse of UV Photodetectors by the Incorporation of Plasmonic Nanoparticles on GaN Through the Resonant Coupling of Localized Surface Plasmon Resonance. *Nano-Micro Lett.* **2020**, *12*, No. 91.

(17) Luo, L. B.; Zeng, L. H.; Xie, C.; Yu, Y. Q.; Liang, F. X.; Wu, C. Y.; Wang, L.; Hu, J. G. Light trapping and surface plasmon enhanced high-performance NIR photodetector. *Sci. Rep.* **2014**, *4*, No. 3914.

(18) Cho, C. Y.; Zhang, Y. J.; Cicek, E.; Rahnema, B.; Bai, Y. B.; McClintock, R.; Razeghi, M. Surface plasmon enhanced light emission from AlGaIn-based ultraviolet light-emitting diodes grown on Si (111). *Appl. Phys. Lett.* **2013**, *102*, No. 211110.

(19) Butun, S.; Cinel, N. A.; Ozbay, E. LSPR enhanced MSM UV photodetectors. *Nanotechnology* **2012**, *23*, No. 444010.

(20) Clavero, C. Plasmon-induced hot-electron generation at nanoparticle/metal-oxide interfaces for photovoltaic and photocatalytic devices. *Nat. Photonics* **2014**, *8*, 95–103.

(21) Wang, Y.; Ge, C. W.; Zou, Y. F.; Lu, R.; Zheng, K.; Zhang, T. F.; Yu, Y. Q.; Luo, L. B. Plasmonic Indium Nanoparticle-Induced High-Performance Photoswitch for Blue Light Detection. *Adv. Opt. Mater.* **2016**, *4*, 291–296.

(22) Zorić, I.; Zach, M.; Kasemo, B.; Langhammer, C. Gold, Platinum, and Aluminum Nanodisk Plasmons: Material Independence, Subradiance, and Damping Mechanisms. *ACS Nano* **2011**, *5*, 2535–2546.

(23) West, P. R.; Ishii, S.; Naik, G. V.; Emani, N. K.; Shalae, V. M.; Boltasseva, A. Searching for better plasmonic materials. *Laser Photon. Rev.* **2010**, *4*, 795–808.

(24) Liu, S. X.; Wang, T.; Chen, Z. Z. High-Performance of Al Nanoparticle Enhanced 4H-SiC MSM Photodiodes for Deep Ultraviolet Detection. *IEEE Electron Device Lett.* **2017**, *38*, 1405–1408.

(25) Bao, G. H.; Li, D. B.; Sun, X. J.; Jiang, M. M.; Li, Z. M.; Song, H.; Jiang, H.; Chen, Y. R.; Miao, G. Q.; Zhang, Z. W. Enhanced spectral response of an AlGaIn-based solar-blind ultraviolet photodetector with Al nanoparticles. *Opt. Express* **2014**, *22*, 24286–24293.

(26) Yan, X.; Ji, X.; Wang, J.; Lu, C.; Yan, Z.; Hu, S.; Zhang, S.; Li, P. Improve photo-to-dark current ratio of p-Si/SiO₂/n-Ga₂O₃ heterojunction solar-blind photodetector by inserting SiO₂ barrier layer. *J. Vac. Sci. Technol., B: Nanotechnol. Microelectron.: Mater., Process., Meas., Phenom.* **2022**, *40*, No. 052207.

(27) Husham, M.; Hassan, Z.; Selman, A. M.; Allam, N. K. Microwave-assisted chemical bath deposition of nanocrystalline CdS thin films with superior photodetection characteristics. *Sens. Actuator, A* **2015**, *230*, 9–16.

(28) Razeghi, M.; Rogalski, A. In *Semiconductor Ultraviolet Detectors*, Conference on Photodetectors - Materials and Devices; Spie - Int Soc Optical Engineering: San Jose, BELLINGHAM, 1996; Vol. 2685, pp 114–125.

(29) Yang, W. F.; Zhang, F.; Liu, Z. G.; Wu, Z. G. Effects of annealing on the performance of 4H-SiC metal-semiconductor-metal ultraviolet photodetectors. *Mater. Sci. Semicond. Process* **2008**, *11*, 59–62.

(30) Chiou, Y. Z. DC and Noise Characteristics of 4H-SiC Metal-Semiconductor-Metal Ultraviolet Photodetectors. *Jpn. J. Appl. Phys.* **2004**, *43*, No. 2432.

(31) Lu, Y. F.; He, H.; Liu, S. X.; Chen, Z. Z. Effects of annealing treatment on the high temperature performance of 4H-SiC metal-semiconductor-metal ultraviolet photodiodes. *Mater. Sci. Semicond. Process* **2017**, *71*, 116–120.

(32) Lee, S. K.; Zetterling, C. M.; Östling, M.; Åberg, I.; Magnusson, M.; Deppert, K.; Wernersson, L.-E.; Samuelson, L.; Litwin, A.

Reduction of the Schottky barrier height on silicon carbide using Au nano-particles. *Solid-State Electron.* **2002**, *46*, 1433–1440.

(33) Pratiyush, A. S.; Krishnamoorthy, S.; Solanke, S. V.; Xia, Z. B.; Muralidharan, R.; Rajan, S.; Nath, D. N. High responsivity in molecular beam epitaxy grown beta-Ga₂O₃ metal semiconductor metal solar blind deep-UV photodetector. *Appl. Phys. Lett.* **2017**, *110*, No. 221107.

(34) Zhang, W.; Xu, J.; Ye, W.; Li, Y.; Qi, Z. Q.; Dai, J. N.; Wu, Z. H.; Chen, C. Q.; Yin, J.; Li, J.; et al. High-performance AlGaIn metal-semiconductor-metal solar-blind ultraviolet photodetectors by localized surface plasmon enhancement. *Appl. Phys. Lett.* **2015**, *106*, No. 021112.

Recommended by ACS

High-Performance Flexible GaAs Nanofilm UV Photodetectors

Zhi-Xiang Zhang, Lin-Bao Luo, et al.

MAY 25, 2023
ACS APPLIED NANO MATERIALS

READ 

Schottky Junction Made from a Nanoporous Au and TiO₂ Film for Plasmonic Photodetectors

Bingwu Liu, Jiawen Hu, et al.

MARCH 14, 2023
ACS APPLIED NANO MATERIALS

READ 

Plasmonic Light Scattering via Au Nanoparticles for Extended Photo Absorption in InGaIn/GaN Multiquantum Wells for Unbiased Stable Solar-Driven Water Splitting

Ameer Abdullah, Sang-Wan Ryu, et al.

JANUARY 08, 2023
ACS APPLIED NANO MATERIALS

READ 

Design and Fabrication of High-Efficiency, Low-Power, and Low-Leakage Si-Avalanche Photodiodes for Low-Light Sensing

Amita Rawat, M. Saif Islam, et al.

MAY 04, 2023
ACS PHOTONICS

READ 

Get More Suggestions >